Beach Wizard: Nearshore bathymetry estimation through assimilation of model computations and remote observations

Ap van Dongeren [a,*], Nathaniel Plant [b], Anna Cohen [a], Dano Roelvink [a,c], Merrick C. Haller [d], Patricio Catalán [d,e]

[a] *Deltares (formerly Delft Hydraulics), Delft, The Netherlands*
[b] *Naval Research Laboratory, Stennis Space Center, MS, USA*
[c] *Unesco-IHE, Delft, The Netherlands*
[d] *School of Civil and Construction Engineering, Oregon State University, Corvallis, OR, USA*
[e] *Department de Obras Civiles, UTFSM, Valparaiso, Chile*

ARTICLE INFO

ABSTRACT

A data–model assimilation method (called "Beach Wizard") is presented with which the nearshore subtidal bathymetry can be accurately estimated based on video-derived observations of wave roller dissipation and variation of the intertidal shoreline, and/or radar-derived observations of wave celerity. Using many consecutive images, these observed properties are compared with numerical model results, and through a simple, optimal least-squares estimator approach the estimated bathymetry is adjusted gradually for each image in order to improve the fit between model output and observations. The key advantages of the technique are that it is based on multiple sources of information (i.e., different remote sensors and/or data products), depends on only a few free parameters (to which the model results are insensitive), and shows good skill. Herein, the technique is applied to a synthetic case and two sets of field data from sites at Duck, NC (USA) and Egmond (The Netherlands). The method, which may be extended with observations of other properties from other sources than the three described in this paper, can deliver coastal state information (i.e., simultaneous updates of bathymetry, waves, and currents) with high temporal and spatial resolution and can be used in conjunction with or instead of in-situ measured data.

© 2008 Elsevier B.V. All rights reserved.

1. Introduction

Information on the evolving state of the nearshore zone – in terms of the bathymetric variability, surface waves, and circulation patterns – is crucial to shoreline management, protection of the hinterland against flooding, recreational safety, and naval operations. Obtaining this information from in-situ measurements is often not feasible due to costs, logistic limitations, hostility of the surf zone, or the need to obtain the data on short notice.

As an alternative, sophisticated numerical models combined with limited in-situ and remote-sensing data may be used to estimate the state of the nearshore zone. Numerical models that predict the hydrodynamics of these environments are reaching the level of complexity and numerical efficiency needed to resolve the 2- and 3-dimensional wave and flow processes over features such as rip channels and sandbars. When provided with accurate bathymetry and

forcing conditions, the prediction skill of these hydrodynamic models is good (e.g. Sutherland et al., 2004; Van Rijn et al., 2003). Models that couple the hydrodynamics with sediment transport and bathymetric evolution are also nearing operational form (e.g. Lesser et al., 2004). However, forecasts from state-of-the-art surf zone models significantly degrade for prediction horizons exceeding several days, especially when bathymetry is complex and dynamic due to evolving rip channels or other forms of variability. Therefore, one of the most severe limitations in the accurate prediction of waves and currents is the lack of accurate and up-to-date bathymetric information.

Improvement of the model skill, and hence, lengthening of the predictive horizon, may be expected from assimilating observations in near real-time. In that sense, remotely sensed data are of particular interest, because they are synoptic and can be obtained without interference with the environment and with generally less logistical effort. Parameters of interest in the nearshore can be extracted from remotely sensed video (e.g. Holland et al., 1997; Aarninkhof and Holman, 1999) and radar (e.g. Bell, 1999; McNinch, 2007), and include surface currents (Chickadel et al., 2003), wave breaking distributions (Lippmann et al., 1996), wave run-up (Aagaard and Holm, 1989),

shoreline position (e.g. Plant and Holman, 1997; Aarninkhof et al., 2003), nearshore topography (Lippmann and Holman, 1989; Holman et al., 1991; Holland and Holman, 1997; Van Enckevort and Ruessink, 2003a,b), and wave properties (Harbitz, 1994a,b; Stockdon and Holman, 2000). For a recent review on video applications see Holman and Stanley (2007). Although these methods have largely been developed for shore-based applications, airborne platforms have also demonstrated similar capabilities (e.g. Dugan et al., 2001, Piotrowski and Dugan, 2002).

With respect to bathymetry estimation, Stockdon and Holman (2000) used video imagery to obtain the dominant wave frequency and the cross-shore component of the wave number (i.e. the wave phase speed) and used the linear dispersion relation to obtain the local depth. The method performed best outside the surf zone and for low-amplitude swells (i.e. for conditions where linear theory applies). This technique of phase speed based bathymetric inversion was pioneered by Williams (1946), Johnson (1949) and Fuchs (1953) who used time-lapsed aerial photography, and has also been applied by Greidanus (1997) using synthetic aperture radar, Bell (1999) using X band marine radar, and Leu et al. (1999) using SPOT (satellite) images.

In previous work directly related to the present effort, Aarninkhof et al. (2005a) presented a technique to estimate cross-shore bathymetry from time-averaged video imagery using a simple linear relationship between erosion and accretion on the one hand, and the difference between modelled and measured wave roller energy dissipation on the other. Aarninkhof et al. (2005a) demonstrated that the technique is capable of reproducing the dominant morphological changes during the first year of a shoreface nourishment project at a multiple barred beach at Egmond, The Netherlands. The rms error in the estimated bed elevations was approximately 40 cm for the two cross-sections that they considered. Errors on the order of 10 to 20 cm were found at the seaward face of the bars and increased up to 20 to 40 cm near the bar crest. Maximum deviations of up to 80 cm were found in the trough regions, where wave dissipation information was absent.

Aarninkhof et al. (2005b) presented the extension of this method to two horizontal dimensions using the Delft3D modelling system (Lesser et al., 2004) and compared to pilot cases at Monterey, CA, USA and again at Egmond. While this extended method demonstrated the potential to accurately estimate complex bathymetry, the data-assimilation scheme was ad hoc. The limitations of the method were that it required knowledge of some parameters that are typically unknown, that only one input data stream could be utilized (i.e. the video-derived wave dissipation estimates), and that the results showed large deviations from ground truth in the bar troughs and near the shoreline. Finally, a recent example of bathymetry estimation via data assimilation is given by Scott and Mason (2007) who integrated an estuarine morphodynamic model with observations of the nearshore morphology (intertidal bathymetry in their case) using similar data-assimilation techniques to those used herein. Their method improved the predictive performance of their model at Morecambe Bay, England

The objective of this study is to describe and demonstrate an improved data-assimilation scheme (hereafter called Beach Wizard). In applications to two field sites we will show that the scheme provides robust, reasonably accurate, and smooth estimates of the seasonal and storm-induced variations of the bathymetry. Our approach to this is to derive an improved, statistically optimal 2DH assimilation method, extend the number of remote-sensing data sources from one to multiple sources, and reduce the number of free parameters relative to the model of Aarninkhof et al. (2005a,b). The sources that are added are video-derived intertidal bathymetry and radar-derived wave celerities. In addition, the uncertainties in the bathymetric estimates are quantified. Preliminary results from this method were presented in Cohen et al. (in press).

The new method is validated against a synthetic case and applied to two field sites: one at Duck, NC (USA) for a short-term (10 day) hindcast and the other at Egmond, The Netherlands for a long-term (18 month) hindcast. This paper is outlined as follows: in Section 2 the data-assimilation model formulation is given. The model is verified with a synthetic example in Section 3. Section 4 describes the field data sources and in Section 5 the model is applied to two field cases, followed by the Discussion and Conclusions.

2. Data-assimilation model formulation for bathymetric updates

The model formulation uses an optimal least-squares estimator (Bouttier and Courtier, 1999) to update the bathymetry. It needs the prior state of the bathymetry h_{prior} (and its uncertainty σ_{prior}) as well as new estimates of bathymetry h_{obs} which we will obtain indirectly from remote-sensing observations (and their uncertainty σ_{obs}). The updated bathymetry can then be computed as

$$h_{\mathrm{update}} = h_{\mathrm{prior}} + \alpha(h_{\mathrm{obs}} - h_{\mathrm{prior}}) \tag{1}$$

where all quantities are functions of space unless otherwise noted. The optimal weighting α of the prior and observed estimates is given by

$$\alpha = \left(\frac{\sigma_{\mathrm{prior}}^2}{\frac{T_s}{\Delta t} \sigma_{\mathrm{obs}}^2 + \sigma_{\mathrm{prior}}^2} \right), \tag{2}$$

which will have values between 0 and 1. This weighting term balances the impact of the uncertainties in the prior bathymetry and in the observations. While the formulation is clearly similar to Kalman's (1960) weighting, this equation is used here in a time-update scheme, which means that the same observation is used for every time step in the simulation. Since these observations are not statistically independent, the value of σ_{obs}^2 needs to be multiplied by a factor $T_s / \Delta t$, where T_s is the simulation duration for a given image and Δt the numerical time step. Finally, the uncertainty of the updated depths can be computed simultaneously with Eq. (1) as

$$\sigma_{\mathrm{update}}^2 = \alpha \frac{T_s}{\Delta t} \sigma_{\mathrm{obs}}^2. \tag{3}$$

where the updated values in Eqs. (1) and (3) will become the prior values in the next time step.

As mentioned above, we do not have direct observations of the bathymetry. Instead, we have remote-sensing observations of wave celerity and/or time-averaged image intensity, and we have prior estimates of these quantities obtained from a forward hydrodynamical model and the prior estimate of the bathymetry. Thus, we must use an inverse model to relate the remotely sensed observations to the bathymetry. Using the chain rule

$$h - h_{\mathrm{obs}} = \left(\frac{\mathrm{d}f}{\mathrm{d}h} \right)^{-1} (f - f_{\mathrm{obs}}) \tag{4}$$

where f_{obs} is an observed (measured) local quantity and f is a computed quantity. Here f may be read as wave dissipation, wave celerity and/or measured (intertidal) bathymetry. Using Eq. (4), the time-update scheme (1) becomes

$$h(t + \Delta t) = h(t) - \alpha \frac{\frac{\mathrm{d}f}{\mathrm{d}h}}{\left(\frac{\mathrm{d}f}{\mathrm{d}h} \right)^2 + \delta^2} (f - f_{\mathrm{obs}}) \tag{5}$$

where variables in Eqs. (1)–(3) with subscript "update" are at time level $t + \Delta t$ and all variables with subscript "prior" are at time level t. Instead of the derivative $\left(\frac{\mathrm{d}f}{\mathrm{d}h} \right)^{-1}$ we have used an inverse transfer function (Menke, 1989) with a noise level δ, which ensures that the denominator does not go to zero when the derivative is zero. Note that we are not inverting the co-variance matrix that describes the

sensitivity of variables at one location to variables at other locations, but instead we only consider the main diagonal terms which describe co-located data inputs and model outputs. Continuous results are enforced through the forward wave modelling with the hydrodynamical model Delft3D. Using the above formulation the update scheme will converge gradually to the correct bathymetry driven by an arbitrarily large model–data mismatch. If α were constant and non-zero, the convergence would be exponential. The weighting term damps this convergence based on the quality of the observations. We must estimate this term in the face of both potentially poor knowledge of the remote-sensing system error characteristics and knowledge that the physical process model itself contains error. Thus, we have implemented the inversion scheme such that a large model–data mismatch will reduce the value of α. We do this by allowing a large mismatch to increase the uncertainty in the observed data (we don't trust it because it is far from the solution that we already have). The balance is that the correct bathymetry is approached quasi-linearly.

This uncertainty in the observed data σ_{obs}^2 will be defined as the ratio of two quantities. The first is the sum of the measurement error and the difference between the modelled and observed quantity, and the second is the square of the gradient with respect to depth, or

$$\sigma_{obs}^2 = \frac{\varepsilon^2 + (f - f_{obs})^2}{\left(\frac{df}{dh}\right)^2 + \delta^2}, \tag{6}$$

where ε is the measurement error for a given source (in units of the quantity of that source) and δ is again the noise level. This equation states that the uncertainty is large when the difference between the modelled and observed quantities are large (i.e. the computational bed level must deviate considerably from ground truth) or the gradient is small (the quantity is not dependent on the local depth; hence, it gives no reliable information about the bed level).

This assimilation model (5) is generalized for multiple sources as

$$h(t + \Delta t) = h(t) - \alpha \sum_{i=1}^{S} \frac{\frac{df_i}{dh}}{\left(\frac{df_i}{dh}\right)^2 + \delta_i^2} (f_i - f_{i,obs}), \tag{7}$$

where the index i indicates the source. For the present application we have limited the number of sources to three: wave roller energy dissipation, wave celerity, and intertidal bathymetry. These sources may be extended with any measurable quantity that can be expressed as a differentiable function of depth, such as percentage of breaking or wave height.

The uncertainty per source $\sigma_{obs,i}^2$ is given by Eq. (6) with subscript i on all variables, and the total uncertainty in observations (in units of bed level) is the ensemble of the uncertainties of the individual sources or

$$\sigma_{obs}^2 = \frac{1}{\sum_{i}^{S} \left(\frac{1}{\sigma_{i,obs}^2}\right)}, \tag{8}$$

where the double reciprocal is applied so that the source with the smallest uncertainty is locally dominant. Eqs. (2) and (3) remain the same for multiple sources.

The assimilation scheme is applied to consecutive (in time) sources, e.g. a sequence of video or radar images from which the observed wave properties and their uncertainties are derived. Initial values of h_{prior} and σ_{prior} at the start of the first simulation are also required, which can be derived from a previous assimilation run, a recent bathymetric survey, or a best guess. The simulation for a source at a given time uses the updated bathymetry from a previous simulation as a starting value. The uncertainty in this bathymetry is also taken from the previous run,

except that the uncertainty is increased as a function of the (calendar) time that has elapsed between images because of possible morphological changes. In other words, the certainty we have obtained using a set of data should degrade over time when no new data are available. The uncertainty increase between the end result of one simulation and the start of another is heuristically modelled as a sigmoid function, which is equivalent to an exponential approach toward σ_{evo} with an initial taper so that the increase in uncertainty is not large over a short time after the last data was applied.

$$\sigma^2(t_j) = \sigma^2(t_{j-1}) + (\sigma_{evo}^2 - \sigma^2(t_{j-1})) \tanh^2\left(\frac{3}{T_r}(t_j - t_{j-1})\right). \tag{9}$$

Here j is the index of the run (image), and t_j the Julian day. The time scale T_r controls the rate at which the computed uncertainty is dominated by morphological change and evolves into the natural uncertainty σ_{evo}. The time scale constant must depend on the magnitudes of sediment transport rates that are responsible for beach evolution and, hence, must vary with the wave height or currents. For instance, near sand bars, T_r is on the order of days, while offshore it may approach zero if there is no expected bathymetric change over the analysis time period. However, we will use a constant value of 5 days, which is representative of the average conditions. We have chosen σ_{evo} to be identical to the initial prior bathymetry (σ_{prior}) at 1 m, which eliminates one parameter and corresponds to an upper limit in the bar variability at Duck (see Fig. 6 of Plant et al. 1999).

The method has only one free parameter, the simulation length T_s, as opposed to the scheme proposed by Aarninkhof et al. (2005a,b), which involved two free parameters per source. The present method also needs the measurement error field ε_i, which is a property of the remotely sensed data and consequently is not a freely tunable parameter. Also, as mentioned above, the model needs an initial (best guess) bathymetry and an initial uncertainty. We will perform sensitivity tests for these parameters in the Discussion section. In the present formulation we have done away with the concept of a virtual buffer layer of suspended sediment as used in Aarninkhof et al. (2005a,b). This choice implies that the present model does not necessarily conserve mass, although this constraint could be included straightforwardly by forcing the incremental updates to have a zero spatial mean. Moreover, if there is a known change in mass due to a beach nourishment, this could be imposed on the solution.

The assimilation model is implemented in the Delft3D morpho-dynamical model and can be run alone or in parallel with a physics-based morphology model. For the present purpose, modelled morphological evolution due to sediment transport is turned off in order to focus on the assimilation results. Delft3D computes the spatial distribution of the roller energy dissipation and wave celerity (the properties f), as well as the derivatives $\frac{df}{dh}$ across the model bathymetry using the observed wave and tide conditions (water level, wave height, peak period, and wave angle). This is done in the wave roller routine (Roelvink, 1993; Reniers et al., 2004), which concurrently solves the energy equations of the organized wave motion and the roller motion using the expressions for the wave and roller energy dissipation given by Baldock et al. (1998) and Reniers et al. (2004), respectively. We refer to Reniers et al. (2004) for details of the model equations. However, since the derivative of roller dissipation with respect to depth cannot be computed analytically, we have used the derivative of the organized wave dissipation with respect to depth as a proxy. This replacement will introduce a small spatial offset (since the dissipation of organized wave dissipation triggers the development of the roller) but on the scales we are interested in here this is allowable. The details of the computation of the derivatives are given in Appendix A.

Each simulation runs in stationary mode, which means that the water level and offshore wave conditions are assumed constant for the
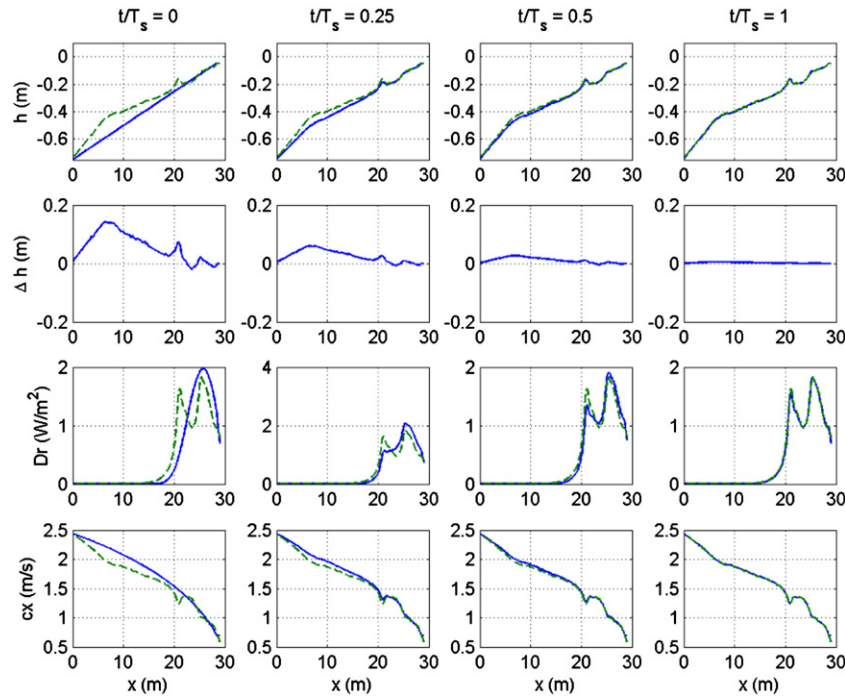
Fig. 1. Top row: evolution of the computed bed level (solid line) and target bathymetry (dashed line); second row: difference between computed bed level and target; third row: computed (solid line) and "measured" (dashed line) roller dissipation; bottom row: computed (solid line) and "measured" (dashed line) celerity. The columns indicate four time instances (t/T_s=0, 0.25, 0.5 and 1).

duration of the simulation (about 2 h maximum). The boundary conditions therefore consist of tidal elevation, offshore H_{rms} wave height, peak period, and mean direction. In hindcast mode these quantities can be derived from nearby gauges and buoys. Depending on data availability, for some simulation runs data from only a single source are used, and while in other runs concurrent data from multiple sources are used. In order to properly compute the bed evolution, it is necessary to perform a large number of sequential simulation runs (on the order of 50 to 100 in our applications) for a diverse set of combinations of wave conditions and water levels so that the driving force for the bed update can be applied all along the sub- and intertidal bathymetry.

3. Verification with synthetic case

The assimilation model is validated against a synthetic case of a longshore uniform, barred bathymetry taken from the Boers (1996) fixed-bed flume experiments, which were a scaled-down version of the large-scale LIP experiments (Arcilla et al., 1994). From the set of wave conditions we have selected case 1C (with wave parameters H_{rms}=0.073 m, T_{m01}=2.25 s), which has a high incident wave steepness and wave breaking occurring both over the bar and near the shoreline.

First a target run is performed on the actual bathymetry and the steady-state result is taken as the "measured" celerity and roller energy dissipation profile, c_o and D_o, respectively. All other information (including the bathymetry, but not the offshore wave condition) is discarded. The aim is to use the assimilation model starting from an initially plane slope and using the known wave boundary conditions and then determine whether the actual barred bathymetry can be recovered.

Even though the "measured" data is perfect, the model is run with measurement error values of ε_D=0.2 W/m² and ε_c=0.25 m/s, which is about 10% of the maximum value of D_o and of the mean value of c_o, respectively, and is a realistic noise level. After the hydrodynamics reach a steady-state the bottom update routine is invoked at t/T_s=0. Fig. 1 shows the evolution of the computed bed level (top row, solid lines) towards the target (dashed lines) for four time instances. The

update is driven by the difference between the computed (solid lines) and "measured" (dashed lines) roller energy dissipation (third row) and celerity (bottom row). These differences are seen to decrease over time as the solution converges. This is confirmed by the evolution of the differences in the computed bed level and the target bed level in the second row, which decrease over the duration of the simulation by a factor of 10. The differences do not go to zero due to the inclusion of the measurement errors and the finite length of the simulation T_s.

4. Real world data sources

4.1. Roller energy dissipation

Estimates of wave roller dissipation are derived from plan view Argus video time-exposure images of breaking intensity. Oblique time-exposure images, sampled from one or more video cameras that cover the area of interest are merged and rectified into a synoptic, plan view image (e.g. Fig. 2). The dissipation quantification procedure largely follows Aarninkhof et al. (2005b) and assumes that video intensity is a proxy for wave roller dissipation (see the Discussion section regarding the impact of errors in this assumption.)

To obtain a roller dissipation map from an image, a four-step approach is followed. First a background intensity level is removed from the individual camera images so that the darker, offshore areas
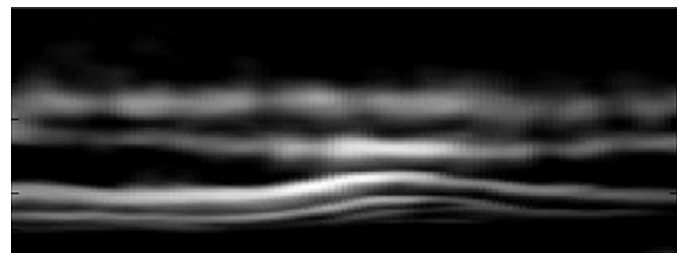
Fig. 2. Merged plan view roller dissipation rate map of Egmond station Jan van Speijk of 13/12/1999 at 10:00 GMT. The shoreline is at the bottom of the figure and white bands indicate areas of wave breaking.

(where no wave breaking occurs) correspond to zero video intensity. Secondly, in order to obtain smooth wave dissipation maps covering multiple cameras, we correct for differences in contrast between individual cameras. Then, the individual camera views are merged into a plan view, roller dissipation map I_v which typically covers a coastal stretch up to a few kilometres alongshore. Finally, the corrected image intensities are scaled such that they are a quantitatively correct measure of roller dissipation. To that end, we normalize I_v so that the total normalized intensity in the model domain is equal to unity, and scale the normalized intensity map with the incoming wave energy flux to obtain a video-derived measure of roller dissipation D_o

$$D_0(x,y) = \left(\frac{I_v(x,y)}{\int_x \int_y I_v \mathrm{d}x\mathrm{d}y} \right) \int_y E c_g \cos\theta \mathrm{d}y \qquad (10)$$

where the wave energy at the offshore boundary of the model is defined as, $E = 1/8\rho g H_{rms}^2$, c_g is the wave group velocity, and θ is the wave angle of incidence with respect to shore normal. The resulting roller dissipation map for one time instance is shown in Fig. 2.

4.2. Intertidal bathymetry

Intertidal beach bathymetries are generated with the Intertidal Beach Mapper (IBM, Aarninkhof et al, 2003). The IBM determines the three-dimensional beach surface between the low-tide and high-tide shoreline contours by mapping a series of beach contours derived from video images and sampled throughout a tidal cycle (see also Plant et al., 2007). IBM delineates a shoreline feature from time-averaged video imagery on the basis of the visual contrast between the sub-aerial and sub-aqueous parts of the beach. The corresponding shoreline elevation is estimated from the tide and wave conditions at the time of image collection. Validation of IBM against a dataset of GPS-surveyed shorelines has shown that mean vertical model deviations increase with increasing distance from the video station and are less than 15 cm along the Egmond area (Aarninkhof et al., 2003).

Application of IBM over a single tidal cycle yields a dataset of shoreline sample points with variable sample spacing. The alongshore sample distance ranges from 1 to 15 m, depending on the pixel resolution, and varies inversely with distance from the video station. The cross-shore sample distance varies between 1 and 20 m and is governed by the local beach slope, the water level change between successive video images, and the possible occurrence of emerging intertidal bars. Shoreline sample points are interpolated to a grid with a cross-shore spacing of 2 m and an alongshore spacing of 20 m.
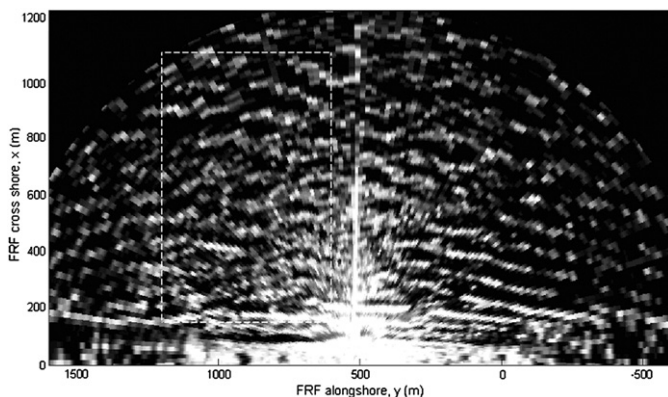

Fig. 3. Single radar image (Sept. 28, 2005), radar located onshore at center of semi-circle. Waves appear as bright linear features. The shoreline is at the bottom. The dotted box denotes the location of the minigrid.

4.3. Wave celerity

Wave celerities can be estimated from video pixel time series (e.g. Stockdon and Holman, 2000) or from marine radar image sequences (e.g. Bell, 1999). In the present application we obtained wave celerities using radar, but only at the Duck, NC (USA) location. The raw radar data consists of a sequence of 640 images collected at 0.73 Hz. The footprint of each image is a semi-circle of 1200 m radius centered at the base of the FRF pier (see Fig. 3). Image sequences were collected once per hour over a period of 5 days. Further details of the radar system and data collection can be found in Lentine (2006).

In order to estimate wave celerities from these data, the raw image data is first converted from the range and azimuth coordinates in which it was collected to the Cartesian grid corresponding to the model domain. Spatial maps of the cross-shore component of wave celerity are obtained from the Cartesian data using the Complex Empirical Orthogonal Function method (Wallace and Dickinson, 1972; Stockdon and Holman, 2000). These maps are processed first by counting the number of outlier values that exceed a threshold value, defined as the sum of the alongshore mean celerity and one alongshore standard deviation. We found that the results for the entire set of maps had a bimodal distribution. Either a map had few percent outliers or the map had a large percentage of outliers. Poor quality maps were identified by the number of outliers exceeding 30%, and were not used further. Gaps left by any removed data in the remaining maps were filled in by interpolation. For the assimilation method an additional criterion imposed was that only celerity maps demonstrating quasi-alongshore uniformity were considered. This was done by calculating the cross-shore average of the ratio of the alongshore standard deviation to the alongshore mean celerity. The value of this quantity should not exceed 30%. An example of raw (with outliers removed) and interpolated celerity maps is shown in Fig. 4.

5. Application to field cases

5.1. Duck, NC, USA

The model was applied to the (so-called "minigrid") area north of the pier of the U.S. Corps of Engineers Field Research Facility (FRF) at Duck, NC (USA) for the period of 21–29 September 2005. This microtidal beach (tide range of less than 1 m) on the Mid-Atlantic coast is exposed to swell from hurricanes to the south and north-east storms. The nearshore morphology typically includes one or two sandbars.

Three different data sources were available for validation of the present assimilation approach: video-derived wave roller dissipation and intertidal bathymetry, and radar-derived wave celerity. Using approximately 50 time-exposure images, dissipation maps were constructed following the procedure described above. A set of 4 intertidal bathymetries was also generated based on time-exposure images over the period 26/09/2005 until 29/09/2005. In addition, six wave celerity maps covering both sides of the FRF pier were used from the period of interest. The measurement errors were chosen at $\varepsilon_D = 20$ W/m^2 for the dissipation, $\varepsilon_c = 1$ m/s for the celerity, and $\varepsilon_S = 0.5$ m for the error in the intertidal bathymetry, respectively. The first two values are about 10% of the maximum of the observed property, and the latter error is an upper limit of the error found by Aarninkhof et al. (2003).

The spatial domain of the numerical model spans from 200 to 1200 m in the y-direction (alongshore) and from 100 to 900 m in the x-direction (cross-shore) in the local FRF coordinates. However, the present analysis will focus on the minigrid area, where independently surveyed bathymetric data are available. The assimilation starts with an arbitrarily chosen bathymetry from October 1994, i.e. prior information that is more than a decade out of date. The model is run for consecutive intervals with a duration of 1 or 2 h, depending on the time interval between images. At the offshore boundary, short wave energy and peak period (group speed) are imposed using buoy observations at 8 m of water depth. The lateral
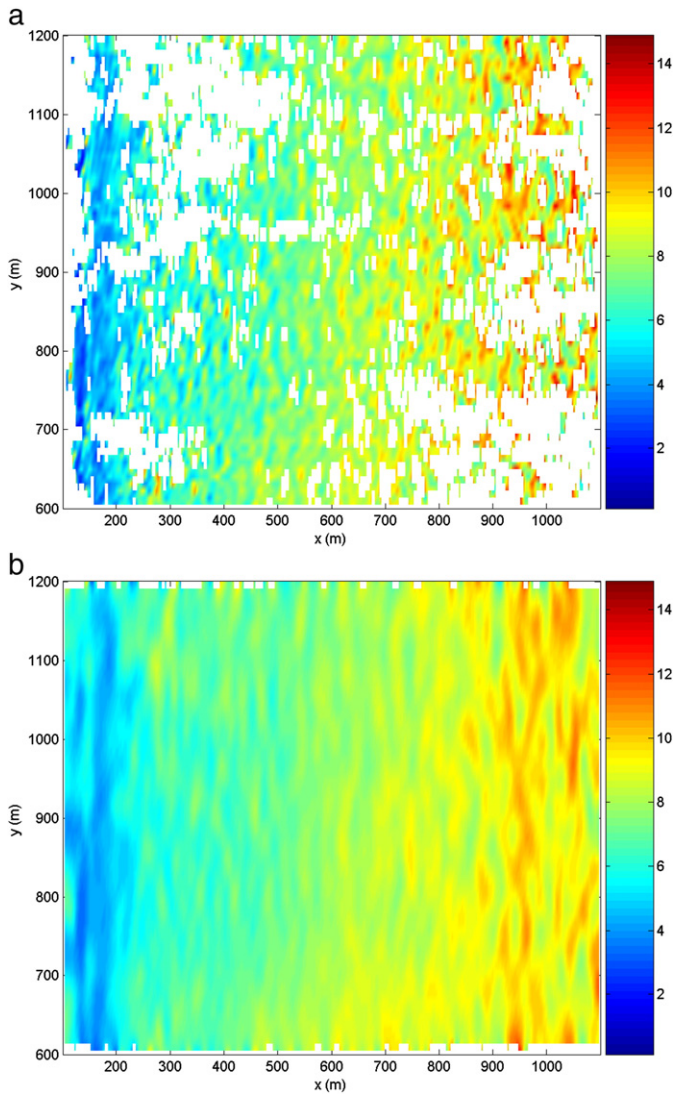
a

b

Fig. 4. Left: radar-derived celerity map and right: celerity map after interpolation. Values of the celerities are in m/s. The shoreline is to the left.

boundaries are prescribed by the Neumann boundary condition $\left(\frac{\partial}{\partial y} = 0\right)$ (Roelvink and Walstra, 2004). The tide level is assumed constant over each simulation run and is provided by the tide gauge mounted on the pier. The flow and wave model were calibrated on Duck 1994 data. From this calibration, a breaking parameter $\gamma = 0.65$ (using the definition by Battjes and Stive, 1985) is derived.

The results are shown in Figs. 5 and 6. The time history of the H_{m0} wave heights (Fig. 6, top panel) shows that the period included one major and one minor storm. The assimilation is performed using 50 stationary runs divided over the interval of which five are shown in Fig. 5, and are indicated by the dots and the plus symbol in Fig. 6. The dots are runs with wave dissipation images; the plus symbol indicates one of the runs with both wave dissipation and celerity images. In Fig. 5 the bathymetric evolution is shown for two cross-sections (at $y = 800$ and $y = 1100$ m in the local FRF coordinate system) with the uncertainty (Eq. (2)) indicated by the error bars. The updated bathymetry (solid red line) evolves from the initial 1994 bathymetry (dashed red line), to the bathymetry measured on 21 September 2005 at the start of the simulation period (solid blue line). This final bathymetry shows significant alongshore variability and is also, presumably, evolving slowly in time.

The top two rows of panels in Fig. 5 show that the bathymetry first adjusts in the area where there is wave dissipation, which is near the

shore since the waves are low. Due to many successive images the error estimates (with an initial value at the start of the simulation of $\sigma_{\text{prior}} = 1$ m) decrease most where dissipation occurs, since this is the region that is sensitive to bathymetry changes. Periods of low wave heights (top row of Fig. 6) result in slight increases in the update error, since it is assumed that the actual bathymetry may evolve (Eq. (9)), but there is no dissipation information available to reduce this source of uncertainty. The storm of the 25th of September provides wave dissipation information in the region $x = 200–400$ m so that the bathymetry can be updated confidently there (Fig. 5 third row). The celerity information updates the bathymetry furthest offshore, and also reduces the uncertainty (fourth row). The bottom row of panels in Fig. 5 shows the end result over this simulation period. At the cross-section at $y = 1100$ m the modelled and measured bathymetry agree very well except in the trough at $x = 250$ m. The error estimate generally makes an accurate prediction of the maximum differences between the updated and independently measured bathymetry (an overestimate of the uncertainty at locations offshore of the bar is due to our lack of consideration of the spatial variability of bathymetric evolution, which is much lower than our assumed error). At the $y = 800$ m cross-section the measured bar at $x = 175$ m is not predicted in the right location but shifted landwards in the form of a terrace and lies outside the error bands. If the bathymetry is Gaussian-distributed 64% of the ground-truth data should fall into this band.

The bottom panel of Fig. 6 shows the rms errors in the entire domain and in sub-domains of the inner and outer surf zone and the shoaling zone. The overall error (solid line) and the error in the outer surf zone (dashed line) are decreasing quite steadily over the simulation period. The error in the inner surf zone (dash-dotted line) is constant and increases temporarily after the storm (because the observations are insensitive to the bathymetry at this time, while we assume that the true bathymetry continues to evolve). The error in the shoaling zone (dotted line) decreases only slightly. Overall the total rms error is reduced from 0.8 to 0.3 m.

The utility of the assimilation scheme is further evaluated using the Brier Skill Score, defined by

$$\text{BS} = 1 - \frac{\overline{(h_{\text{m}}(t_{\text{end}}) - h_{\text{obs}})^2}}{\overline{(h_{\text{m}}(t_0) - h_{\text{obs}})^2}} = 0.85 \tag{11}$$

where $h_{\text{m}}(t_{\text{end}})$ and $h_{\text{m}}(t_0)$ are the final and initial model bathymetries, and h_{obs} is the ground-truth bathymetry of September 21. This score is higher than the reported score of 0.3 by Scott and Mason (2007) for a different type of coastal bathymetry. It shows that for this case we can resolve 85% of the difference between the initial and true bathymetries using only a short span of data.

5.2. Egmond, The Netherlands

The second application involves the assessment of the evolution of subtidal bathymetry along a 2 km coastal stretch at Egmond (The Netherlands) over an 18 month period starting December 1999 (Aarninkhof et al., 2005b). Egmond Beach is situated on the northern part of the central Dutch coast and is characterized by two shore-parallel subtidal nearshore sandbars. The meso-tidal (ranging between 1.4 and 2 m) beach is exposed to a wave climate with a yearly mean wave height H_{mo} of 1.2 m and a mean period T_{m} of about 5 s, showing considerable seasonal fluctuations.

During the 18 month period, the bathymetry was surveyed twice per year, typically along 50 cross-shore profiles with 100 m spacing alongshore. The measured depth is estimated to have an error of less than 15 cm. Offshore wave conditions were measured with a directional wave buoy at IJmuiden, located approximately 15 km to the south. Approximately 15% of the data was missing, of which half could be replaced by values from an identical buoy approximately
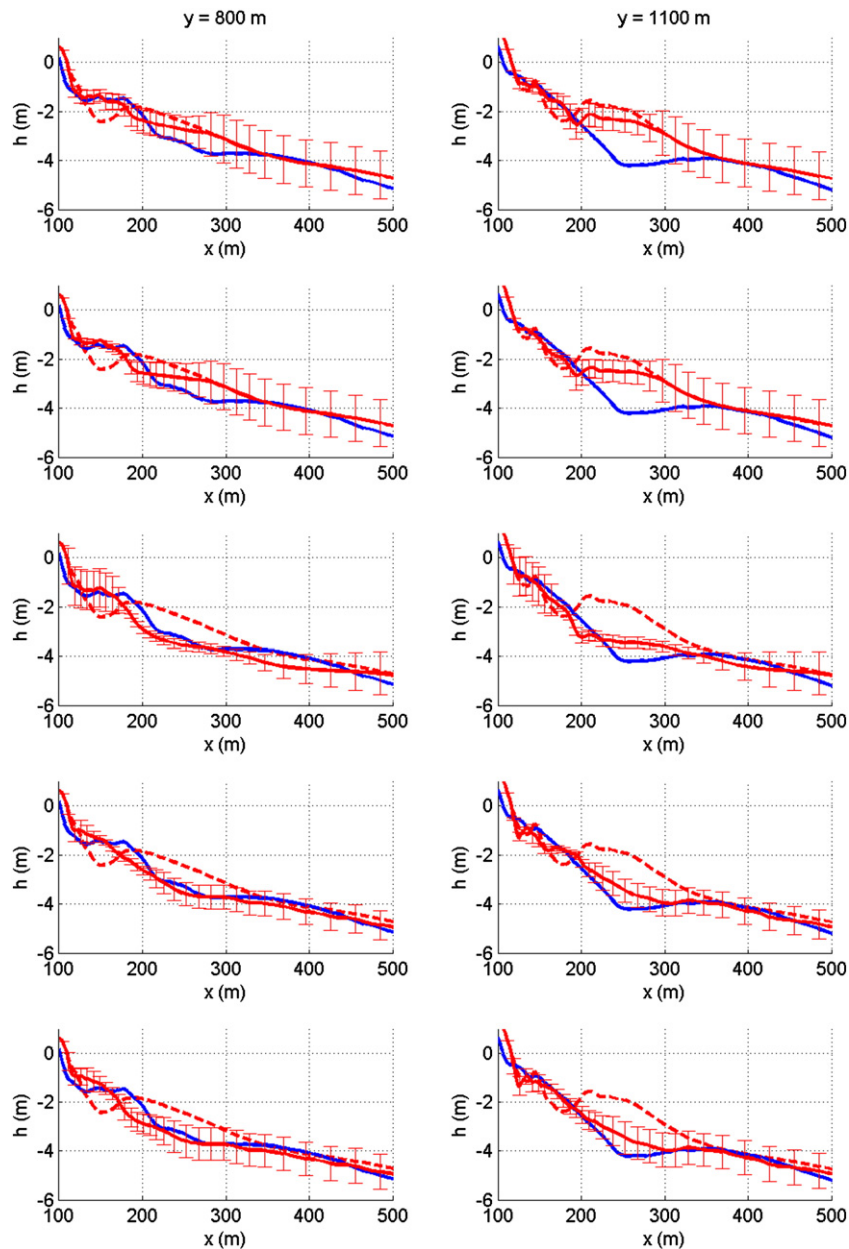
Fig. 5. Computed (solid red line), measured (solid blue line) and initial (dashed red line) bathymetries for two transects at y = 800 and y = 1100 m for five time instances given in Fig. 6.

75 km to the north. Offshore tidal levels are found from interpolation in water level data collected at tidal stations located 15 km north and south of Egmond.

At this location two data sources are available for assimilation during the modelled period: dissipation and intertidal bathymetry from video. We use the 100 wave dissipation maps as generated and used in Wijnberg et al. (2004), collected from 13/12/1999 until 20/07/2001. Intertidal bathymetry files are constructed from the intertidal bathymetries derived from video, using two sets generated by Caljouw (2000) and Nipius (2002). Due to variations in the spatial extent of the two datasets, only the overlapping area of a 1360 m coastal strip centered around the Egmond lighthouse and enclosed by the elevation contours at 0 m NAP and +0.9 m NAP could be used. The overall Egmond dataset obtained consists of 27 intertidal beach bathymetries over the period 15/06/1999 until 22/09/2001.

A model domain was set up similar to that of Wijnberg et al. (2004). The flow model grid spans from −1400 to 1400 m in y-direction

(alongshore) and from −100 to 1200 m in x-direction (cross-shore) in the local Argus coordinate system. The grid sizes Δx and Δy are 5 and 20 m respectively. The model is run for each 2 h period where remote-sensing information is available. The simulation starts with a bathymetry measured on 14 and 15 September 1999. At the offshore boundary, short wave energy and peak period (group speed) are imposed, the lateral boundaries are prescribed by the Neumann boundary condition. Wave directions are calculated by a SWAN model, which is laterally extended with respect to the flow grid, to avoid boundary disturbances on the flow grid. The model and instrument error settings were the same as was used in the Duck hindcast.

Fig. 7 shows the results of the Egmond application for one cross-shore array (at y = 10 m in the local coordinate system and corresponding to JARKUS (Dutch acronym for "Annual Coastal Surveys", see e.g. Van Koningsveld and Lescinski, 2007). The actual bathymetry was measured only five times during the simulation period. The measured bathymetry is indicated in blue (solid line) and
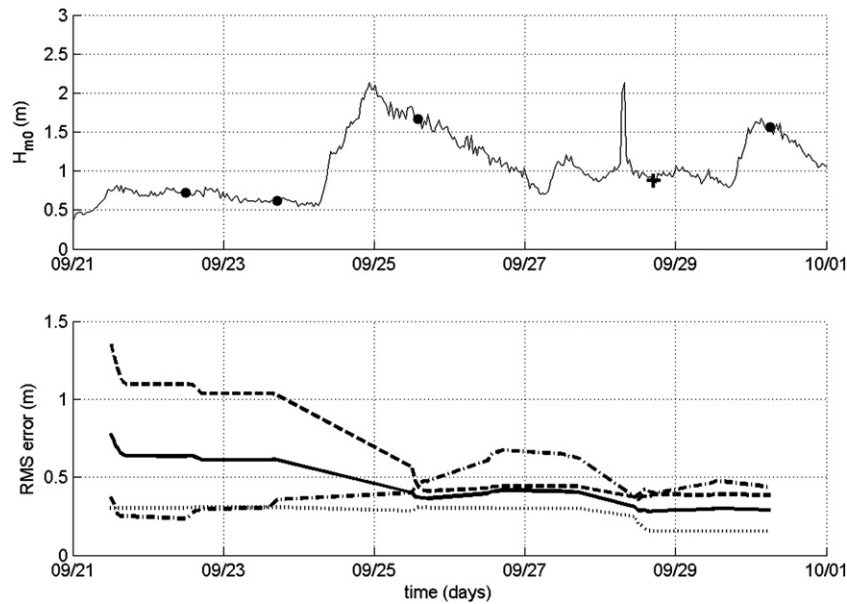
Fig. 6. Top panel: Time history of the offshore H_{m0} wave height. The dots indicate the pictured time instances with only wave dissipation images. The plus indicates an instance with both wave dissipation and celerity field images. Bottom panel: the rms error between computed and measured bathymetries. The solid line is the error in the entire domain between $x = 150$ and $x = 500$ and $y = 800$ and $y = 1200$ m. The dash-dotted line is the error in the inner surf zone ($150 < x < 200$ m), the dashed line is the error in the outer surf zone ($200 < x < 300$) and the dotted line is the error in the shoaling zone ($300 < x < 500$ m).

the computed bathymetry in red (solid line). Initial values of both are shown with dashed lines. The computed uncertainty estimates are shown as the red error bars.

Again, the assimilation approach yields bathymetric updates that converge toward the independently measured values (Fig. 7). In the deeper regions (seaward of $x = 700$ m) the bathymetry is less dynamic. No useful assimilation data in this region is available, so the model does not update the bathymetry. The model-predicted errors (Fig. 7) vary in a manner similar to that seen in the Duck example. The error is smallest around the bar tops. Errors in the deeper regions (troughs and offshore) remain larger, because of the lack of sensitivity to the data in these areas. In order to decrease these errors, inclusion of a third data source (for instance wave celerity) would be needed. For the model period, unfortunately no such data were available.

The 2-D results (Fig. 8) show that the rms error over the entire model domain is about 0.5 m. The largest differences between the measured and computed bathymetry occur seaward of the shoreline, where the depth is overpredicted. The former approach (Aarninkhof et al., 2005b, not shown) resulted in an rms error of about 1.5 in the same model domain, which was due to much larger deviations in the deeper regions and just seaward of the shoreline. This shows that the current assimilation method has improved the performance near the shoreline by including intertidal bathymetry as an assimilation source in the model. Also, the performance near the shoreline is improved because the overall performance in the bar-trough region is improved and the accumulation of errors towards the beach has decreased. Still, the model skill is lowest in these shallow areas.

6. Discussion

The assimilation model has shown excellent skill in estimating the nearshore and intertidal bathymetry. The approach also produces estimates of the uncertainty in the bathymetry, which reflects both the sensitivity to the data and true bathymetric evolution. These results depended on the accuracy of several parameter choices that describe the errors that are inherent to this assimilation problem. These choices required information in addition to the remote-sensing data themselves and deserve further discussion.

Parameter settings: The model requires a few initial conditions and parameter settings. The measurement error, ε_i, was unknown and an ad hoc value of 10% of the maximum of the measured value was used. While this seems to be a reasonable noise level, we tested the sensitivity of our results by increasing the error value to 25% of the maximum. Fig. 9 (dashed line) shows a very similar, yet more gradual reduction of the rms error in comparison with the original (10%) run (solid line). In essence, increasing the data error reduces the impact of the data and convergence of the bathymetric update proceeds more slowly.

The simulation length T_s for a given image has a default of 1 h (the default time between images) with a maximum of 2 h, corresponding to the maximum duration of hydrodynamic stationarity. The sensitivity of the results to this parameter setting is studied by using a value of 30 min for the Duck case. The result (Fig. 9, dash-dotted line) is almost identical to the default run. The effect of the initial condition σ_{prior} (set equal to σ_{evo}) is studied by reducing its value from 1 to 0.5 m, which means that the initial bathymetry is taken as more trustworthy, and may be less sensitive to the input from the remote-sensed data. The results (Fig. 9, dotted line) are again very similar to the default run. The model results are thus fairly insensitive to reasonable settings of the parameter values. This indicates model robustness and predictive capability. The primary impact of selecting the correct error parameters would be an improvement in the updated bathymetric uncertainty.

Dependence on initial bathymetry: We have shown that the updated bathymetry converges toward the true bathymetry even when an outdated initial bathymetry is used to begin the assimilation. It appears, however, that there can be lasting impacts of an inaccurate initial bathymetry near the shoreline. This is a result of our neglecting to consider the spatial co-variance of the updated bathymetry and error. In comparison to the measured bathymetry the results show that there are two forms of systematic estimation errors. The first is an erroneous building of a nearshore terrace in the bathymetric estimate (at Duck). The second is the erroneous deepening near the shoreline ("digging"). Both effects are due to the same problem, namely that the bathymetric adjustment in the subtidal area is governed by the spatial distribution of wave dissipation. Over a trajectory from offshore to onshore, the wave dissipation has a history, which is not entirely
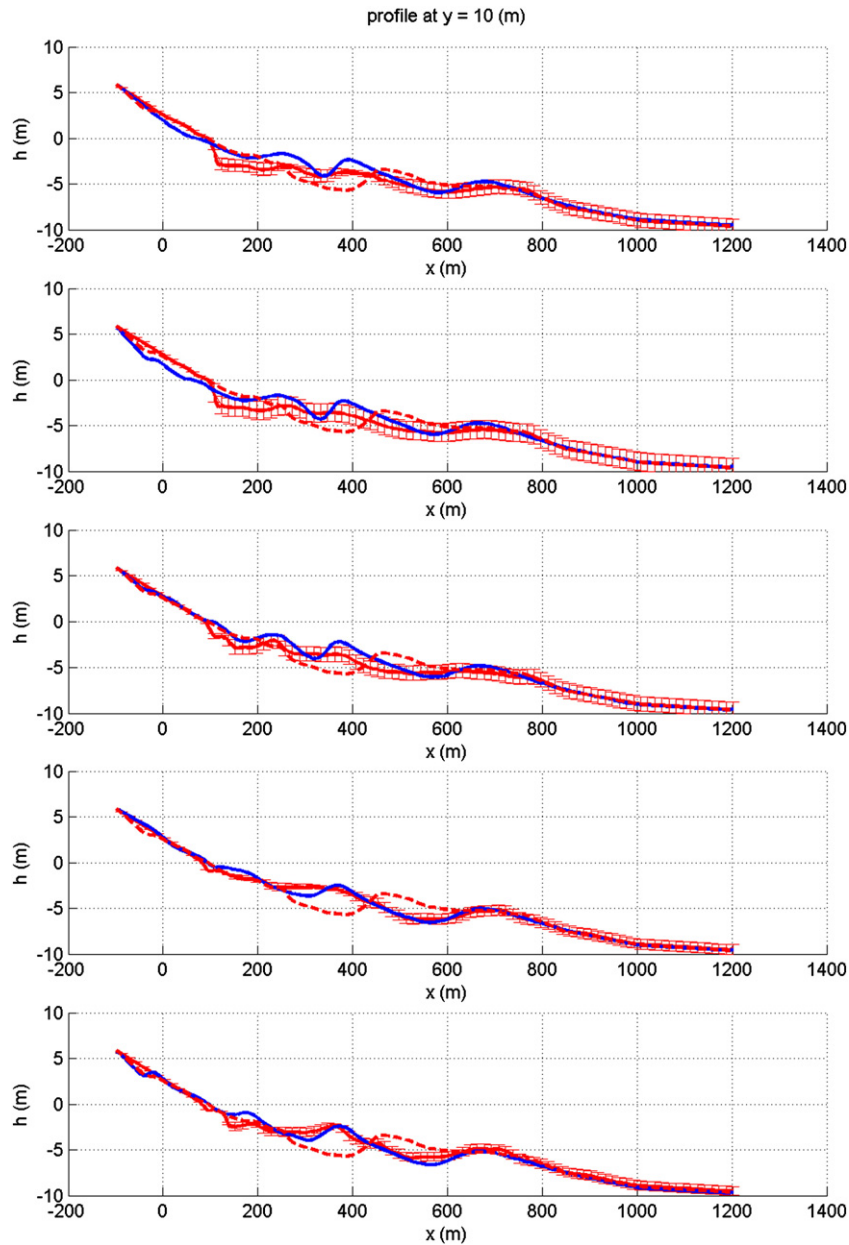
Fig. 7. Results of the Egmond application at a cross-shore array (*y* = 10 m) at five points in time during the model period when the bathymetry was measured (from top to bottom: 05/04/2000, 17/05/2000, 17/09/2000, 18/04/2001 and 18/06/2001). The blue line indicates the measured bathymetry, the red line indicates the computed bathymetry. Dashed lines indicate the initial situation of both. The model-predicted errors are shown in red bars.

accounted for by adjusting the bathymetry due to local differences. For example, if in the true bathymetry a large bar exists, which is not present (yet) in the computational bathymetry, the model will correctly react by raising the bar in that area. However, due to the dissipation over the bar in reality, there will be less dissipation left in the nearshore area. There, the model will react by increasing the local depth, which is possibly incorrect, see Fig. 10.

The solution to this problem is to not use dissipation in the extreme shallow depth where this problem is the largest, but to use another source such as the celerity of the broken waves. The video data necessary to do this is presently being collected at Egmond. However, no such data was available for the period covered in this paper.

Trough behavior: At the end of the Egmond application, the assimilation model starts to fill in the trough at *x* = 300 m. The cause for this is that the video images show a "tail" of dissipation landward of the bar at *x* = 400, whereas the computed dissipation does not. This difference generates an upward driving force landward of the bar, and thus an

underprediction of the depth in the trough. This tail may indicate the presence of persistent high-intensity foam on the sea surface, which is not associated with active wave breaking and is erroneously attributed to wave dissipation by the methodology. This problem could be solved by incorporating a 2D version of the 1D approach by Aarninkhof (2003).

Image selection: The images which are fed to the model are currently hand-selected. This is a laborious process to reject (video) images with sun glare and rain drops on the lens. These effects would give a false indication of areas with high intensity which would be interpreted as areas with breaking waves. While the system is rather robust, a "false" image would nudge the updated bathymetry away from truth and would require a lot (order 10) of "good" images to nudge the bathymetry back. We note that image selection procedures are needed because the image-derived estimates of celerity and dissipation are not provided with accurate data quality estimates. It is apparent from our systematic approach that quantitatively accurate error estimates of all inputs would yield improved assimilation results.
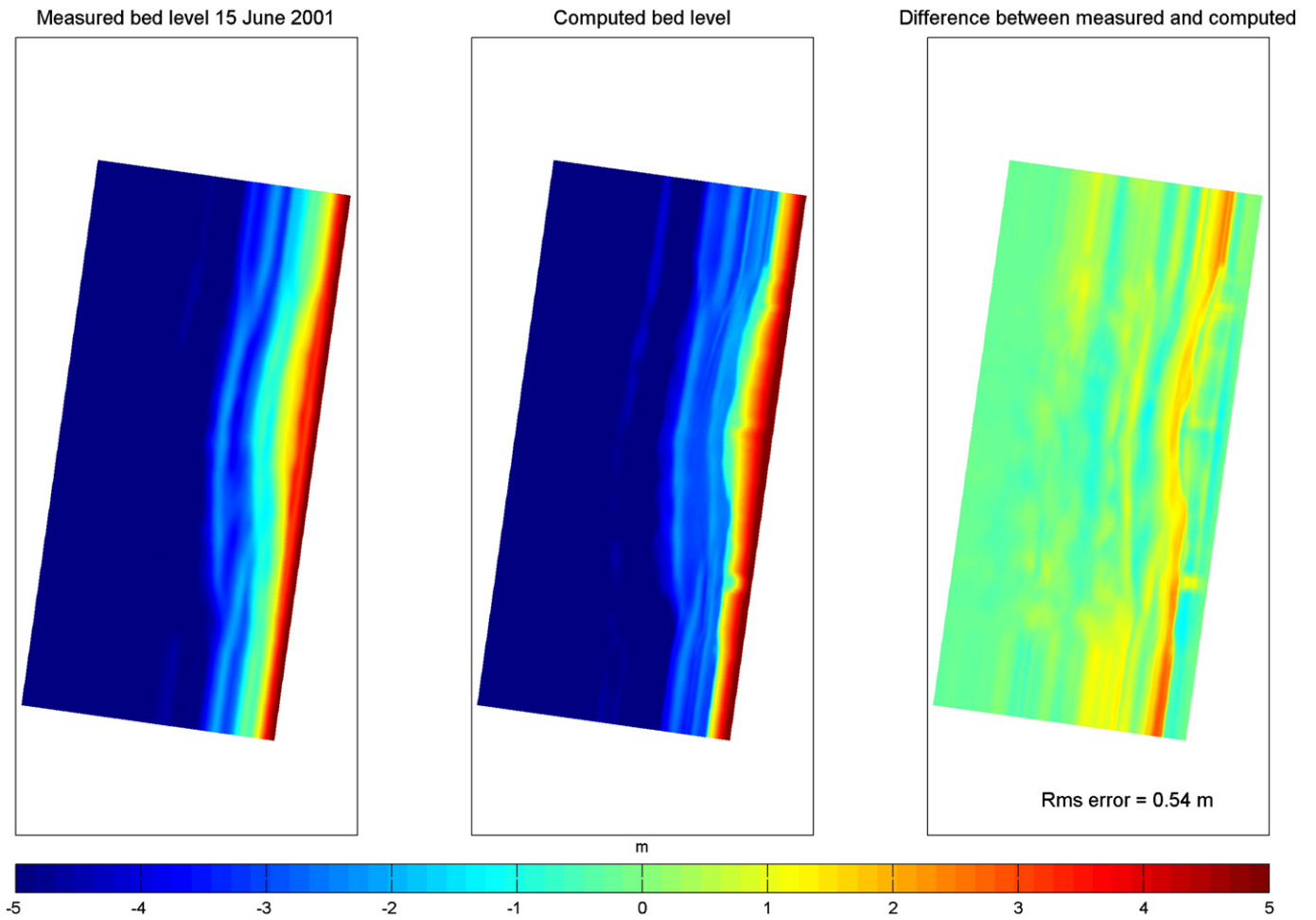
Fig. 8. Results of the Egmond application in the model domain on 15 June 2001. The left panel shows the measured bathymetry. The center panel shows the computed bathymetries with the present model. The difference between the measured and computed bathymetries is shown in the right panel.
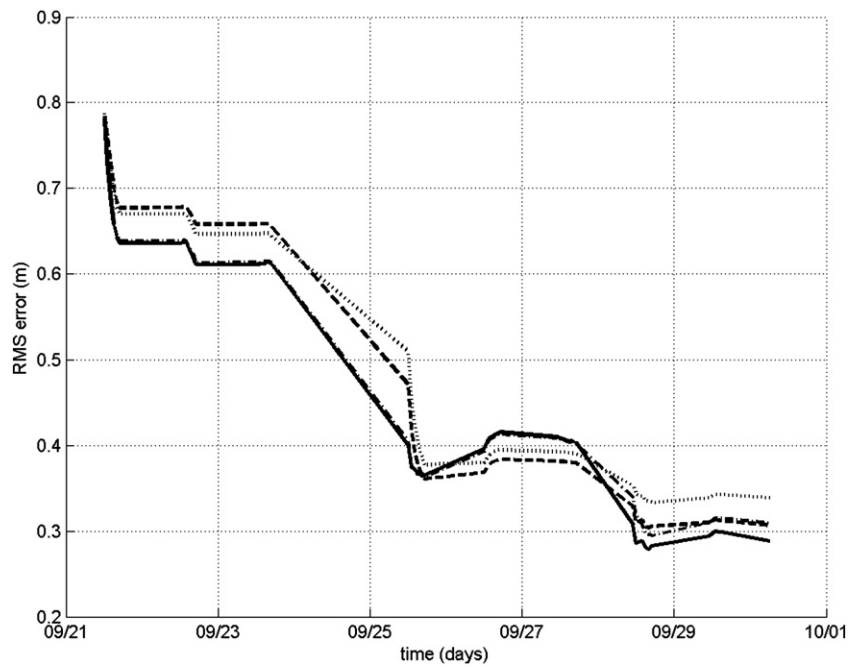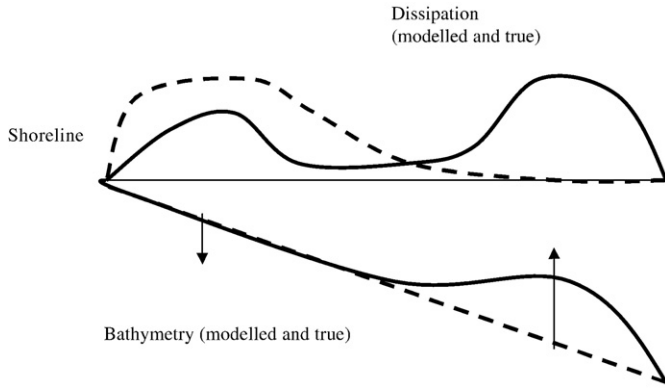

Fig. 9. Sensitivity of bathymetric errors to parameter choices. Solid line: default run; dashed line: increased measurement error; dash-dotted line: reduced simulation length; dotted line: reduced initial uncertainty.

Fig. 10. Schematic of a barred bathymetry (bottom solid line) and associated dissipation (top solid line), and the modelled bathymetry (bottom dashed line) and the modelled dissipation (top dashed line). The arrows indicate the direction of the adjustment of the modelled bathymetry.

Prior error parameterizations: We have implemented an ad hoc estimate of the error on the basis of knowledge of the response of various sections of the bathymetry to waves and currents (Eq. (9)). A better parameterization of the crude T_r parameter in this equation would include a space-dependent parameter which depends on wave height and period reflecting present understanding of sediment transport and bathymetric change. This sort of improved parameterization essentially adds system knowledge to the model. This paper provides a proof-of-concept of the assimilation approach and includes all of the ingredients required for accurate bathymetric updating. It is clear, now, that some of the ingredients deserve further attention.

7. Conclusions

In this paper an assimilation model is presented that is capable of estimating the sub- and intertidal bathymetry based on the difference between remotely sensed quantities of the roller energy dissipation rate, wave celerities and intertidal bed elevation and the corresponding computed quantities for a large number of time instances. The present method is an improvement over the previous method by Aarninkhof et al. (2005a,b) because of the use of a formal inverse model with fewer free parameters and the incorporation of wave celerity and intertidal bathymetry in addition to roller energy dissipation, all of which make the model more robust and reduces the overall error to about 0.3–0.5 m (rms). Moreover, error estimates of the bathymetry are computed. The simulations show that the model-predicted bathymetry falls within +/− one standard deviation of the observed (in-situ measured) bathymetry.

The application to the Duck case shows that over a short time span (including one major storm) the model is capable of predicting the bathymetry accurately given a sequence of remotely observed inputs. The model was then applied to the longer term (1½ year) case at the multi-barred beach of Egmond, where the model (using the same settings) was also capable of predicting the profile change. Finally, tests that varied the tunable (within limits) parameters show that the model results for the Duck case are fairly insensitive to settings of the measurement error, the simulation length, and the initial uncertainty.

Acknowledgements

Appendix A

The bed update routine (Eq. (7)) requires the computation of the gradients $\frac{\mathrm{d}f_i}{\mathrm{d}h}$ for every source. For the three sources considered in this paper the evaluation is as follows

A.1. Celerity

In the case of celerity we substitute $f=c$ and compute

$$\frac{\mathrm{d}c}{\mathrm{d}h} = \frac{\mathrm{d}}{\mathrm{d}h}\left(\sqrt{\frac{g}{k}\tanh(kh)}\right) \tag{A1}$$

using the linear dispersion relation in which k is the wave number at the peak frequency. Taking the derivatives with respect to h, and after some manipulation we find

$$\frac{\mathrm{d}c}{\mathrm{d}h} = \frac{2\pi f_p}{\cosh kh \, \sinh kh + kh} \tag{A2}$$

where f_p is the peak frequency.

A.2. Roller dissipation

In the case of roller dissipation we substitute $f=D_r$. However, the derivative $\frac{\mathrm{d}D_r}{\mathrm{d}h}$ cannot be computed analytically and we will use derivative of the organized wave dissipation with respect to h, so $\frac{\mathrm{d}D_w}{\mathrm{d}h}$ as a proxy. For the dissipation rate of organized wave motion we use the dissipation formula of Baldock et al. (1998). The computation of the derivative is straightforward by chain rule

$$\frac{\mathrm{d}D_w}{\mathrm{d}h} = \frac{\mathrm{d}D_w}{\mathrm{d}\Gamma}\frac{\mathrm{d}\Gamma}{\mathrm{d}H_b}\frac{\mathrm{d}H_b}{\mathrm{d}h} \tag{A3}$$

where

$$\begin{aligned} D_w &= 0.25\rho g f_p H_{rms}^2 \mathrm{e}^{-\Gamma}(1+\Gamma) \\ \Gamma &= \left(\frac{H_b}{H_{rms}}\right)^2 \\ H_b &= \frac{0.88}{k}\tanh\left(\frac{\gamma kh}{0.88}\right) \\ \gamma &= 0.29 + 0.76kh. \end{aligned} \tag{A4}$$

Then

$$\begin{aligned} \frac{\partial D_w}{\partial \Gamma} &= -0.25\rho g f_p H_{rms}^2 \Gamma \mathrm{e}^{-\Gamma} \\ \frac{\partial \Gamma}{\partial H_b} &= 2\frac{H_b}{H_{rms}^2}. \end{aligned} \tag{A5}$$

After some manipulation we find

$$\frac{\partial H_b}{\partial h} = \frac{1}{\cosh^2\left(\frac{0.29kh+0.76(kh)^2}{0.88}\right)}\left[(0.29 + 2*0.76kh) \tag{A6}\right.$$
$$\left.\left(\frac{-kh}{\sinh kh \, \cosh kh + kh}+1\right)\right] + \frac{0.88\tanh\left(\frac{0.29kh+0.76(kh)^2}{0.88}\right)}{\sinh kh \, \cosh kh + kh}.$$

Eqs. (A5) and (A6) are collected and inserted into Eq. (A3).

A.3. Intertidal bathymetry

In the case of observed intertidal bathymetry, we substitute $f = h_s$. The gradient with respect to depth is simply unity.

References

Aagaard, T., Holm, J., 1989. Digitization of wave run-up using video records. Journal of Coastal Research 5 (3), 547–551.

Aarninkhof, S.G.J. (2003). Nearshore bathymetry derived from video imagery, Delft University of Technology, The Netherlands, PhD thesis, 175 pp.

Aarninkhof, S.G.J., Holman, R.A., 1999. Monitoring the nearshore with video. Backscatter 10 (2), 8–11.

Aarninkhof, S.G.J., Turner, I.L., Dronkers, T.D.T., Caljouw, M., Nipius, L., 2003. A video-technique for mapping intertidal beach bathymetry. Coastal Engineering 49, 275–289.

Aarninkhof, S.G.J., Ruessink, B.G., Roelvink, J.A., 2005a. Nearshore subtidal bathymetry from time-exposure video images. Journal of Geophysical Research 110, C06011. doi:10.1029/2004JC002791.

Aarninkhof, S.G.A., Wijnberg, K.M., Roelvink, J.A., Reniers, A.J.H.M., 2005b. 2DH-Quantication of surf zone bathymetry from video. Proc. Coastal Dynamics '05.

Arcilla, A.S., Roelvink, J.A., O'Connor, B.A., Reniers, A.J.H.M., Jimenez, J.A., 1994. The Delta flume '93 experiment. ASCE, Proc. Coastal Dynamics 1994, Barcelona, Spain, pp. 488–502.

Baldock, T.E., Holmes, P., Bunker, S., Weert, P.V., 1998. Cross-shore hydrodynamics within an unsaturated surf zone. Coastal Engineering 34, 173–196.

Battjes, J.A., Stive, M.J.F., 1985. Calibration and verification of a dissipation model for random breaking waves. Journal of Geophysical Research 90 (C5), 9159–9167.

Bell, P.S., 1999. Shallow water bathymetry derived from an analysis of X-band marine radar images of waves. Coastal Engineering 37, 513–527.

Boers, M., 1996. Simulation of a surf zone with a barred beach. Report 1: wave heights and wave breaking. Communications on Hydraulic and Geotechnical Engineering0169-6548.

Bouttier, F., Courtier, P., 1999. Data Assimilation Concepts and Methods. http://www.ecmwf.int/newsevents/training/rcourse_notes/DATA_ASSIMILATION/ASSIM_CONCEPTS/index.html, ECMWF, U.K.

Caljouw, M., 2000. Video-based monitoring of the Egmond beach and shoreface nourishment. Rijkswaterstaat Z2773 RIKZ.

Chickadel, C.C., Holman, R.A., Freilich, M.H., 2003. An optical technique for the measurement of alongshore currents. Journal of Geophysical Research 108 (C11), 3364.

Cohen, A.B., Van Dongeren, A.R., Roelvink, J.A., Plant, N.G., Aarninkhof, S.G.A., Haller, M.C., Catalan, P., in press(2006). Nowcasting of coastal processes through assimilation of model computations and remote observations. Proc. ICCE 2006, in press.

Dugan, J.P., Piotrowski, C.C., Williams, J.Z., 2001. Water depth and surface current retrievals from airborne optical measurements of surface gravity wave dispersion. Journal of Geophysical Research 106 (C8), 16903–16915.

Fuchs, R.A., 1953. Depth Determination on Beaches by Wave Velocity Methods. Univ. of Calif, Berkeley. Rep 74-1.

Greidanus, H., 1997. The use of radar for bathymetry in shallow seas. Hydrographic Journal 83, 13–18.

Harbitz, A., 1994a. Ocean waves measured by a video spot detector. Optical Engineering 33, 2467–2472.

Harbitz, A., 1994b. Video-based ocean wave spectra. Optical Engineering 33, 2473–2479.

Holland, K.T., Holman, R.A., 1997. Video estimation of foreshore topography using trinocular stereo. Journal of Coastal Research 13 (1), 81–87.

Holland, K.T., Holman, R.A., Lippmann, T.C., Stanley, J., Plant, N., 1997. Practical use of video imagery in nearshore oceanographic field studies. IEEE Journal of Oceanic Engineering 22 (1), 81–92.

Holman, R.A., Stanley, J., 2007. The history and technical capabilities of Argus. Coastal Engineering 54, 477–491.

Holman, R.A., Lippmann, T.C., O'Neill, P.V., Hathaway, K., 1991. Video estimation of subaerial beach profiles. Marine Geology 97, 225–231.

Johnson, J.W., 1949. Progress report: wave-velocity method of depth determination by aerial photographs. Tech. Rep. 155-10, Univ. of Calif., Berkeley, 1949.

Kalman, R.E., 1960. A new approach to linear filtering and prediction problems. Transactions of the ASME-Journal of Basic Engineering 82, 35–45 (Series D).

Lentine, J.D., 2006. Nearshore applications of marine radar, M.S. Project Report, Oregon State University. . Available through weblink: http://web.engr.oregonstate.edu/~hallerm/inc/Publications/Lentine_MSProject.pdf.

Lesser, G.R., Roelvink, J.A., Van Kester, J.A.T.M., Stelling, G.S., 2004. Development and validation of a three-dimensional morphological model. Coastal engineering 51 (8–9), 883–915.

Leu, L.G., Kuo, Y.Y., Lui, C.T., 1999. Coastal bathymetry from the wave spectrum of SPOT images. Coastal Engineering Journal 41, 21–41.

Lippmann, T.C., Holman, R.A., 1989. Quantification of sand bar morphology: a video technique based on wave dissipation. Journal of Geophysical Research 94 (C1), 995–1011.

Lippmann, T.C., Brookins, A.H., Thornton, E.B., 1996. Wave energy transformation on natural profiles. Coastal Engineering 27, 1–20.

McNinch, J.E., 2007. Bar and swash imaging radar (BASIR): a mobile X-band radar designed for mapping nearshore sand bars and swash-defined shorelines over large distances. Journal of Coastal Research 23 (1), 59–74.

Nipius, L., 2002. Evaluation of nourishments at Egmond. Rijkswaterstaat, RIKZ, Z2822.51.

Menke, W., 1989. Geophysical Data Analysis, Discrete Inverse Theory. Academic Press, San Diego, USA.

Piotrowski, C.C., Dugan, J.P., 2002. Accuracy of bathymetry and current retrievals from airborne optical time-series imaging of shoaling waves. IEEE Transactions on Geoscience and Remote Sensing 40 (12), 2606–2618.

Plant, N.G., Holman, R.A., 1997. Intertidal beach profile estimation using video images. Marine Geology 140, 1–24.

Plant, N.G., Holman, R.A., Freilich, M.H., Birkemeier, W.A., 1999. A simple model for interannual sandbar behavior. Journal of Geophysical Research 104 (C7), 15,755–15,776.

Plant, N.G., Aarninkhof, S.G.J., Turner, I.L., Kingston, K.S., 2007. The performance of shoreline detection models applied to video imagery. Journal of Coastal Research 23 (3), 658–670.

Reniers, A.J.H.M., Roelvink, J.A., Thornton, E.B., 2004. Morphodynamic modelling of an embayed beach under wave group forcing. Journal of Geophysical Research 109, C01030. doi:10.1029/2002JC001586.

Roelvink, J.A., 1993. Dissipation in random wave groups incident on a beach. Coastal Engineering 19, 127–150.

Roelvink, J.A., Walstra, D.J.R., 2004. Keeping it Simple by Using Complex Models. Advances in Hydro-Science and Engineering, vol. VI. Australia, Brisbane.

Scott, T.R., Mason, D.C., 2007. Data Assimilation for a coastal area morphodynamic model: Morecambe Bay. Coastal Engineering 54, 91–109.

Stockdon, H.F., Holman, R.A., 2000. Estimation of wave phase speed and nearshore bathymetry from video imagery. Journal of Geophysical Research 105, 22015–22033.

Sutherland, J., Peet, A.H., Soulsby, R.L., 2004. Evaluating the performance of morphological models. Coastal Engineering 51, 917–939.

Van Enckevort, I.M.J., Ruessink, B.G., 2003a. Video observations of nearshore bar behaviour. Part 1: alongshore uniform variability. Continental Shelf Research 23, 501–512.

Van Enckevort, I.M.J., Ruessink, B.G., 2003b. Video observations of nearshore bar behaviour. part 2: alongshore non-uniform variability. Continental Shelf Research 23, 513–532.

Van Koningsveld, M., Lescinski, J., 2007. Decadal scale performance of coastal maintenance in the Netherlands. Shore and Beach 75 (1), 20–36 (Winter 2007).

Van Rijn, L.C., Walstra, D.J.R., Grasmeijer, B., Sutherland, J., Pan, S., Sierra, J.P., 2003. The predictability of cross-shore bed evolution of sandy beaches at the time scale of storms and seasons using process-based profile models. Coastal Engineering 47, 295–327.

Wallace, J.M., Dickinson, R.E., 1972. Empirical Orthogonal representation of time series in the frequency domain. Part I: theoretical considerations,. Journal of Applied Meteorology 11 (6), 887–892.

Williams, W.W., 1946. The determination of gradients of enemy-held beaches. Geographical Journal 107, 76–93.

Wijnberg, K.M., Roelvink, J.A., Aarninkhof, S.G.J., 2004. Bed variability in the surf zone at the storm- and seasonal time scale, mapped by Argus-video techniques. Rijkswaterstaat, RIKZ, Z3781.